Comparative analysis of imaging configurations and objectives for Fourier microscopy

JONATHAN A. KURVITS, MINGMING JIANG, AND RASHID ZIA*

School of Engineering and Department of Physics, Brown University, Providence, Rhode Island 02912, USA
*Corresponding author: rashid_zia@brown.edu

Fourier microscopy is becoming an increasingly important tool for the analysis of optical nanostructures and quantum emitters. However, achieving quantitative Fourier space measurements requires a thorough understanding of the impact of aberrations introduced by optical microscopes that have been optimized for conventional real-space imaging. Here we present a detailed framework for analyzing the performance of microscope objectives for several common Fourier imaging configurations. To this end, we model objectives from Nikon, Olympus, and Zeiss using parameters that were inferred from patent literature and confirmed, where possible, by physical disassembly. We then examine the aberrations most relevant to Fourier microscopy, including the alignment tolerances of apodization factors for different objective classes, the effect of magnification on the modulation transfer function, and vignetting-induced reductions of the effective numerical aperture for wide-field measurements. Based on this analysis, we identify an optimal objective class and imaging configuration for Fourier microscopy. In addition, the Zemax files for the objectives and setups used in this analysis have been made publicly available as a resource for future studies. © 2015 Optical Society of America

1. INTRODUCTION

Since the work of Lieb *et al.* [1], Fourier microscopy has become an increasingly important experimental technique for nano-optics. It is now commonly used to study quantum emitters [1–7], optical nanostructures [8–14], and the interactions of these two systems [15–36]. For example, Fourier microscopy has been used to characterize the orientation of single molecules [1,6] and luminescent excitons in layered materials [5], the radiation pattern and directivity of optical antennas [18,30], and the multipolar origin of quantum transitions [3,4,7]. These Fourier microscopy studies all share a common goal, namely, to measure quantitative information about the angular spectrum radiated by a microscopic sample.

However, a surprisingly wide range of optical systems and setups have been used to achieve this goal, including many different objective classes with varying levels of aberration correction and numerical aperture (NA). For example, researchers have used everything from dry objectives with 0.8 NA [34] to 1.49 NA total internal reflection fluorescence (TIRF) objectives [12,13,22,25] and even 1.65 NA high-index objectives [20]. Researchers have also used several different configurations to image the back focal plane (BFP). Some configurations place a Bertrand lens before the microscope's image plane [3–5];

others place a Bertrand lens after the image plane [7,27], while a third set uses relay optics to reimage and magnify the BFP [12,21,29,30,37].

Beyond nano-optics, Fourier microscopy is also becoming an important tool for wide-field imaging and structured illumination applications. Recently, techniques have been developed to reconstruct high-resolution wide-field images from multiple Fourier-space measurements [38]. In addition to imaging, Fourier-space techniques are also being used for optical trapping. For example, by leveraging the Fourier transform properties of an objective, researchers have shown how spatial light modulators can be used to simultaneously trap many particles in arbitrary 3D configurations [39,40].

Adapting optical microscopes to Fourier-space imaging and manipulation can introduce unexpected challenges. For example, even the simple task of focusing in Fourier space can lead to counterintuitive results. Whereas real-space alignment can be readily achieved by focusing on fine features in the image, such fine features in Fourier space are generally the product of aberrations (e.g., distortion near the pupil edge). In this context, Fourier microscopy raises a number of design choices that are distinct from real-space imaging. Specifically, most commercially available objectives and configurations have been

optimized for different real-space applications, yet it is unclear which of these corrections is most important for quantitative Fourier imaging and also to what extent the optics for Fourier imaging will introduce additional aberrations.

The purpose of this paper is to systematically evaluate the optical design choices and experimental parameters inherent in Fourier microscopy, including which microscope objectives are best suited for Fourier imaging, the ideal collection method, and the relative advantages of different Bertrand lens configurations. To quantitatively examine these design choices, we first model complete microscope systems in Zemax. Detailed information about commercial microscope objectives and tube lenses are inferred by the examination of published patents from Nikon, Olympus, and Zeiss. (As a potential resource to readers, we provide Zemax files for all optical elements as well as the combined systems in Ref. [41].) Based on ray-tracing analysis, we show that the ideal objective for Fourier microscopy is a plan-corrected apochromat with a high numerical aperture and low magnification. Furthermore, we show that placing the Bertrand lens into the "infinity" space between the objective and tube lens can yield significant imaging improvements.

2. INTRODUCTION TO FOURIER MICROSCOPY

Fourier microscopy typically involves three basic components: a microscope objective, a tube lens, and a Bertrand lens. This paper focuses on the application of Fourier imaging to modern microscopes, where an infinity-corrected microscope objective is used in combination with a tube lens to produce an image of the object at the exit port of the microscope. The addition of a Bertrand lens allows one to image the Fourier transform of the object by effectively reimaging the objective's BFP. In this way, the tube lens and Bertrand lens can be seen as a two-lens optical system used to image the objective's BFP. For the

purpose of this paper, we assume that the Bertrand lens will be a standard achromatic doublet designed for visible wavelengths. The term Bertrand lens is generally used to describe a lens that performs a Fourier transform without changing the position of the conjugate plane. For simplicity here though, we refer to any lens used to perform a Fourier transform as a Bertrand lens.

As shown in Fig. 1, there are four commonly used configurations for BFP imaging. The first two simply place an achromatic doublet (Thorlabs AC254-050-A and AC254-100-A, respectively) either before [3–5] or after [7,27] the microscope's image plane as shown in Figs. 1(a) and 1(b), respectively. The first configuration typically limits the Bertrand lens to having a focal length of ≤50 mm (due to finite accessible space before the image plane) and is therefore limited in its magnification of the BFP. However, this configuration allows for simple switching between Fourier- and real-space imaging by inserting or removing the Bertrand lens. The second configuration allows for greater magnification of the BFP image, but cannot be used for real-space imaging without additional optics.

The remaining two configurations attempt to overcome these limitations by using relay optics to move the image plane further from the microscope exit port. Figure 1(c) shows a modified 4f relay (Thorlabs AC254-100-A and AC254-050-A), where the second of the two lenses can be replaced by one with twice the focal length to obtain a real-space image [12,21]. The alternate configuration in Fig. 1(d) uses a pair of relaying lenses (Thorlabs AC254-200-A and AC254-150-A) followed by an achromatic pair (Thorlabs MAP104040-A) that can be removed in order to obtain a real-space image [29,30,37]. Although these two designs offer greater flexibility, the additional elements significantly increase alignment difficulty and tolerancing errors. In the following analysis, we will weigh the advantages and disadvantages of these common configurations while also identifying a new approach.
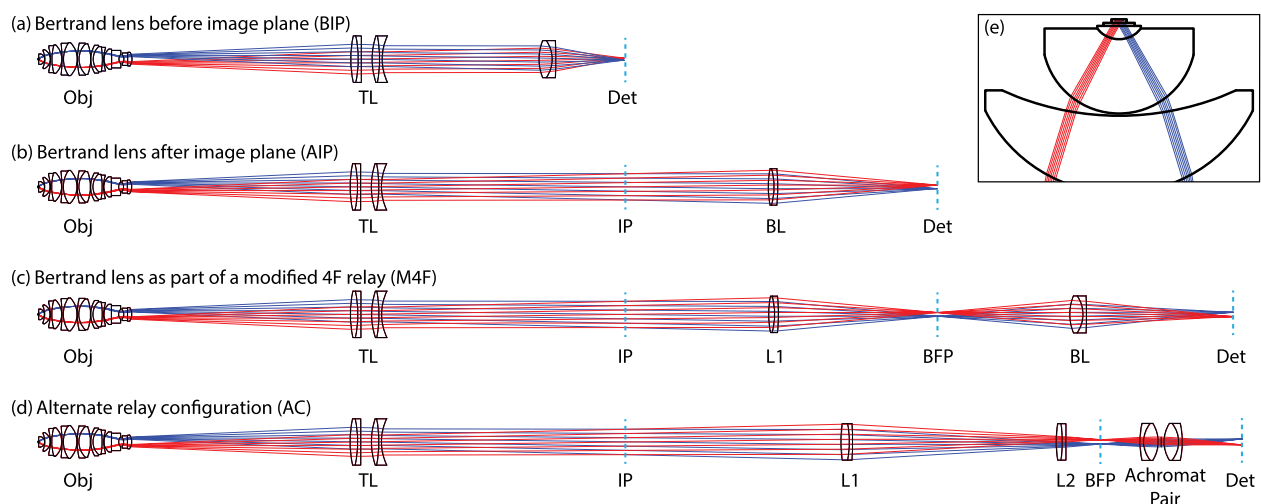

Fig. 1. Schematic of various Fourier imaging techniques showing the relative positions of the objective (Obj), tube lens (TL), image planes (IP), and Fourier imaging optics. In (a) and (b), a single Bertrand lens (BL) is used to image the back-focal-plane (BFP) of the microscope objective onto a detector (Det). In (c), a modified 4f relay is used to magnify the BFP and reimage it further from the microscope. In (d), relay lenses L1 and L2 magnify the BFP image, which is then reimaged onto a detector using an achromatic pair. Blue and red lines show how rays emitted at two different angles (±30°) from the object focus to different locations on the detector plane. (e) A magnified view of the first two elements in the objective highlights the origin of blue and red lines from two different angles.

3. OPTICAL MODELING OF COMMERCIAL MICROSCOPES

Before considering the imaging configurations, it is possible to determine the ideal microscope objective. While microscope manufacturers do not tend to supply consumers with detailed models, their patent applications for objective lenses often specify a great deal of information. These patents often include the radius of curvature, thickness, refractive index, and Abbe number for each optical surface in the objective and associated tube lens. Therefore, by searching the patent literature, it is possible to infer likely designs for commonly used objectives. Although these patents do not include details about any surface coatings used to minimize reflections (and therefore cannot be used to model overall system throughput), they do specify enough information for modeling optical aberrations.

In this section, we provide the rationale by which we examined the patent literature and came to identify likely designs for commercially available components. To guide our search, we have sought to identify patent applications that were submitted near the commercial release date of new objectives, e.g., identifying a 2004 patent application from Nikon [42] describing TIRF objectives with "NA larger than 1.45" that predates the 2005 release of their 1.49 NA TIRF objectives [43]. Wherever possible, we have then tried to use physical examination (i.e., disassembly of objectives and tube lenses) to confirm basic design properties such as the number of elements and their relative curvatures. For every objective examined, we did notice slight discrepancies in specific details, e.g., in the curvatures or thicknesses of some lenses, but discrepancies are to be expected from patent specifications. Despite being sold under the same commercial name, the designs for objectives and tube lenses are presumably subject to continuous improvements and modifications. For example, over the last 20 years, the removal of environmentally hazardous materials from optical glasses (e.g., arsenic, lead, and HCFCs) has required the redesign of many optical components [44]. Nevertheless, we believe these detailed patents are still a helpful source for design optimization, particularly for understanding the differences between objective classes, even if the final objectives may vary from these exact specifications.

A. Glass Determination

Commercial patents generally specify optical materials by their Abbe number and refractive index at the d-line (587.5 nm). With these parameters alone, optical models are only accurate over a relatively small range of wavelengths near the d-line. To enable more accurate analysis over the full visible spectrum, we performed a glass substitution using Zemax's built-in glass catalogs. Where possible, we replaced each material with tabulated data from a "standard" or "preferred" glass with an Abbe number and index identical to the patent specification. If an exact match could not be found for the Abbe number, we looked for the closest match that still provided an exact index match. Where no index match was possible, we simply used the original Abbe number and refractive index. These substitutions greatly improved chromatic aberrations and brought them qualitatively in-line with the spectrally dependent field curvature plots provided in the patents. We further validated this

process by examining the glass manufacturers. For the Zeiss objective, it was possible to use Schott glass for all but one surface. (Carl Zeiss Microscopy and Schott are both subsidiaries of the Carl Zeiss Foundation.) Similarly for Olympus, all but one surface was Ohara glass. (Ohara lists Olympus as one of its major customers [45].) Finally, Nikon objectives appear to use Schott and a variety of Japanese optical glass manufacturers, including its subsidiary Hikari.

B. Tube Lens

The first element we were able to identify in commercial microscopes is the tube lens, because it is a relatively simple component. Since tube lenses are also integral to all infinity-corrected microscope designs, they are often defined in multiple patents. By searching the patent literature, we found numerous patents from Nikon [42,46–55], Olympus [56–62], and Zeiss [63–65] in which the same tube lens was specified for a given manufacturer. In addition, we were able to obtain and disassemble lenses from all three manufacturers. We found that the Zeiss tube lens (Part Number: 452960) matched the single-element design described in objective patents. We also found that the Nikon tube lens for a Ti-U inverted microscope (Part Number: MEA53210-1XL) agrees with the patents in the number of components and their relative curvatures, but component thicknesses differed by ~1 mm. However, the Olympus tube lens (Part Number: U-TLU-1-2) had a different number of elements than the patent specification. Despite these discrepancies, we are confident in the basic designs as they have been listed in many patents spanning several decades and, therefore, seem to be the tube lenses used by the manufacturers to specify the objective performance. In Appendix A, we present the tube lens implementations specified by Nikon, Olympus, and Zeiss patents.

C. Objectives

A number of different objectives were chosen from Nikon, Olympus, and Zeiss based on their availability in the patent literature and in order to cover a large range of NA and aberration corrections. A detailed list of objective manufacturers, magnifications, NA, aberration corrections, and their associated patents can be found in Table 1. Although we cannot be certain that these are exact matches to commercial products, we still believe that the qualitative results obtained from analyzing these patents can help identify the optimal objective class for Fourier imaging.

Table 1. Patent Sources Used for Objective Modeling

U.S. Patent No. [Ref.]	Assignee	Mag.	NA	Class/ Correction
5,517,360 [56]	Olympus	60	1.4	Plan Apo
5,659,425 [58]	Olympus	100	1.65	High-index Apo
6,504,653 [66]	Zeiss	100	1.45	TIRF
6,519,092 [50]	Nikon	60	1.4	Plan Apo
	Nikon	100	1.4	Plan Apo
7,046,451 [42]	Nikon	60	1.5[a]	TIRF
	Nikon	100	1.5[a]	TIRF
7,889,433 [54]	Nikon	60	1.25	Water immersion

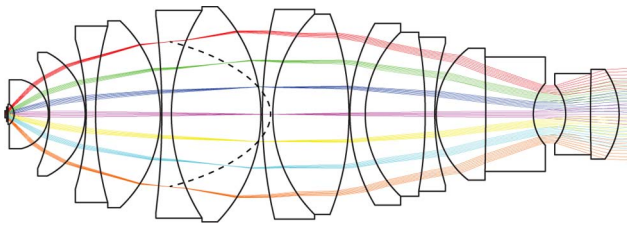[a]Modeled as 1.49 NA to match possible commercial realization.

Fig. 2. Schematic of the 60× objective from the Nikon patent [50]. The full specification, included in Appendix B, contains 23 surfaces corresponding to eight component groups composed of eight glass types. Colored lines represent rays emitted at various angles from the object plane. The dashed black line shows the surface where these rays cross and form a Fourier "plane" inside the microscope objective. Note that this Fourier "back-focal-plane" is a highly curved surface in all the objectives examined here.

To ensure that the Zemax models faithfully represent the patent specifications, we first reproduced the d-line distortion and spherical aberration figures in the patents. As discussed above, we then performed a detailed glass substitution process. This allowed us to confirm the wavelength-dependent spherical aberration plots. Note that the glass substitution procedure does not directly affect our analysis, because we perform all subsequent aberration calculations at the d-line. Nevertheless, we chose to perform the glass substitutions to ensure we correctly modeled the objectives and to create a library of objectives that would be of broader use.

In addition to limited information on the optical glasses that are used, almost none of the patents specify component semidiameters (which are relevant to vignetting). It is not possible with these patent specifications to assume that the objectives could achieve their full NA over the full field of view, because this would require physically impossible lens surfaces, e.g., lenses that intersect other lenses and/or themselves. In order to determine the semidiameters, we allowed these values to float such that the objective collects all the light from an on-axis point source that emits at the specified NA. Using this process, and comparing the resulting semidiameters to patents where semidiameters were specified [56,66], we were able to validate this approach. Specifically, for Ref. [56], there was <2 μm error on all surfaces. For Ref. [66], there was <0.5 mm error on all surfaces and an exact match on the surface that is the primary source of vignetting. For the results of the glass substitution and semidiameter determination, see Appendix B. Figure 2 shows an example of the resulting modeled surfaces from a Nikon 1.4 NA, 60× objective.

4. COMPARATIVE ANALYSIS OF MICROSCOPE OBJECTIVES

A large variety of microscope objectives have been developed for real-space imaging of structures and specimens, each with different optimization metrics in mind. These include apochromatic (low chromatic aberrations), plan (flat field and low distortion), and TIRF (small depth of field) objectives. However, since these were all designed for real-space imaging, their performance for Fourier imaging is not well known. Here, we examine the effect of aberration corrections, nominal

magnification, and numerical aperture as well as the choice of confocal or full-field collection on the quality of the resulting Fourier image.

A. Objective Class and Alignment Sensitivity

When selecting an objective for Fourier-space imaging, it is well known that a great deal of information exists beyond the critical angle for total internal reflection (e.g., NA = 1 for a sample-air interface). Thus, a common approach is to maximize angular collection by using the largest possible NA objective. However, image distortion increases significantly with NA. This is especially true when the NA approaches the refractive index of the immersion medium, $n_{r,imm}$. Indeed, a key measure in the design of high NA objectives is the ratio $NA/n_{r,imm}$. TIRF patents often present their claims in terms of such ratios; for example, Ref. [66] specifies a TIRF objective relative to a $NA/n_{r,imm} > 0.938$ condition. As this number approaches unity and higher angle rays are collected, both aberrations and tolerancing errors are expected to increase.

To examine this effect, we plot in Fig. 3 the apodization factors for the objectives listed in Table 1 as a function of defocusing a Bertrand lens (50-mm achromatic doublet) placed before the image plane. For each objective, distortion data was extracted as a function of Bertrand lens position and apodization factors were calculated according to Ref. [67]. The apodization factor is a dimensionless scaling term that describes how the projected ray density increases with increasing field angle (θ). This factor is derived from the distortion introduced by the optical system, but is generally assumed to be $1/\cos(\theta)$ for systems obeying the Abbe sine condition (i.e., systems with a wide field of view such as microscopes) [1]. Note that the apodization factor was chosen as our metric of objective quality, because it is typically the only correction made to Fourier-space images to take into account the optical setup [1,10,20]. We specifically examine defocus misalignment as it is often the most difficult tolerancing error to correct, because it tends to couple with the distortion in common Fourier microscopy configurations. While decentering and tilt of the Bertrand lens also lead to undesirable changes to the Fourier image, they are relatively easy to observe and correct for even in Fourier space. (For example, by observing fluorescence from an isotropic thin film emitter, tilt and decenter are seen as clear radial asymmetries in the resulting Fourier image, which are readily corrected.) Finally, we chose to use the BIP Fourier imaging configuration shown in Fig. 1(a) due to its simple design, which allowed for easy determination of the objective's influence.

To analyze the results in Fig. 3, consider first the objectives that use a standard ~1.515 refractive index immersion oil. As can be seen from a comparison to the ideal $1/\cos(\theta)$ apodization shown as a dashed black line, the Plan-Apo objectives in Figs. 3(b)–3(d) perform well over the full NA, whereas TIRF objectives in Figs. 3(e)–3(g) perform quite poorly at NA values beyond 1.3. Note that the sharp peaks and sudden drop-off at high NA values are features commonly seen during experimental alignment of the Bertrand lens. Interestingly, the 1.65 NA objective performs quite well, but this is explained by the fact that it uses a high ~1.780 refractive index immersion oil. The high-index 1.65 NA objective thus has a relatively low
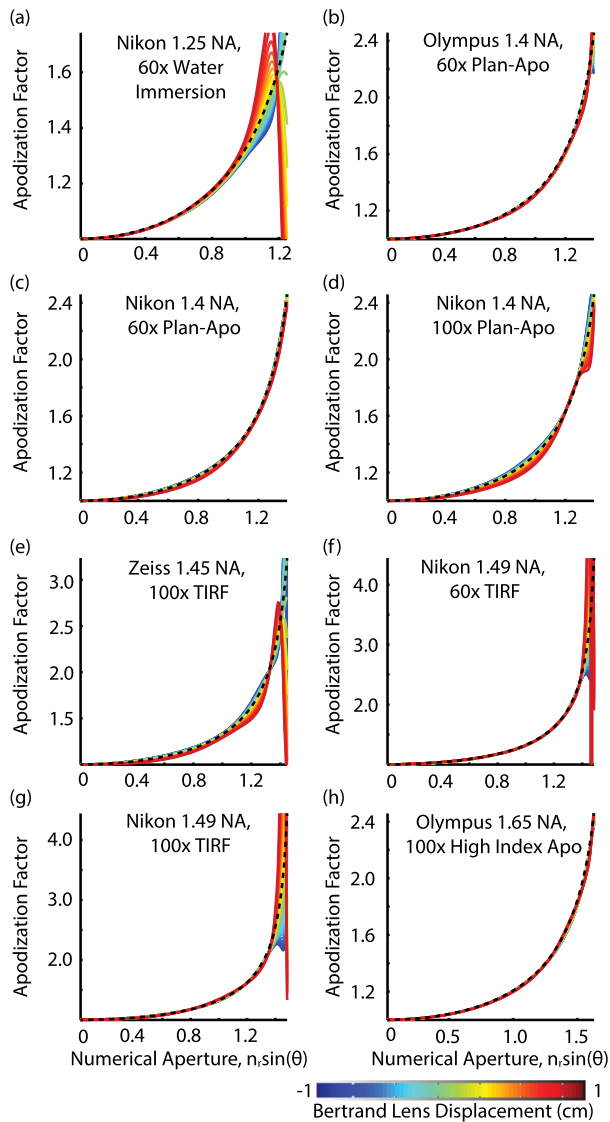
Fig. 3. Apodization factor as a function of BL position in the configuration shown in Fig. 1(a). Significant deviations from the ideal $1/\cos(\theta)$ apodization factor (dashed black line) are seen for TIRF (e)–(g) and high NA water immersion objectives (a), whereas (h) Apo and (b)–(d) Plan-Apo objectives perform well even over a relatively large BL displacement of ± 1 cm.

$NA/n_{r,imm}$ ratio of 0.927, which is comparable to that of the 1.4 NA objectives. In contrast, the 1.25 NA water immersion objective, which has a relatively high $NA/n_{r,imm}$ ratio of ~ 0.938, performs quite poorly. This underscores the point that NA alone may not be the best criteria in selecting an objective for Fourier microscopy. In particular, one should be careful about the use of TIRF and other high $NA/n_{r,imm}$ objectives, especially in applications where a high-NA Plan-Apo objective may be suitable.

For completeness, we note that the objective performance trends discussed above for the BIP configuration were also observed for the AIP configuration in Fig. 1(b) as well as the preferred configuration discussed in Section 5 where the Bertrand lens is placed before the tube lens. While the choice of imaging

configuration does impact the magnitude of tolerancing errors, the Plan-Apo and high-index Apo objectives consistently demonstrated lower tolerancing errors than the TIRF and 1.25 NA water immersion objectives.

B. Magnification and Fourier-Space Resolution

In addition to aberration corrections and NA, magnification is an important parameter for image quality and resolution. For real-space imaging, the choice is fairly obvious. The highest NA and magnification will allow you to resolve the smallest features. However, for Fourier-space imaging, something counterintuitive occurs. For the same NA, you actually obtain a larger Fourier image when using an objective with a lower nominal magnification. To see why, consider the simple schematic shown in Fig. 4 that shows how the Fourier image is formed at the BFP of a single lens. As the focal length is increased (in order to decrease the magnification for a fixed tube lens), the semidiameter must increase in order to maintain the same NA. Thus, as can be seen in Eq. (1) below, the BFP semidiameter height h is inversely proportional to the objective's nominal real-space magnification M specified by the manufacturer,

$$h = \frac{f_t}{M}\left(\left(\frac{n_r}{NA}\right)^2 - 1\right)^{-1/2}, \qquad (1)$$

where f_t is the focal length of the tube lens, n_r is the immersion oil index of refraction, and NA is the numerical aperture of the objective. However, there is still a question as to whether this improves the angular resolution; the image may be larger, but it may also be more blurred out. To demonstrate that this is not the case, we examine the modulation transfer function (MTF) for two comparable systems with differing magnification. (The MTF is defined as the contrast ratio that would be observed at
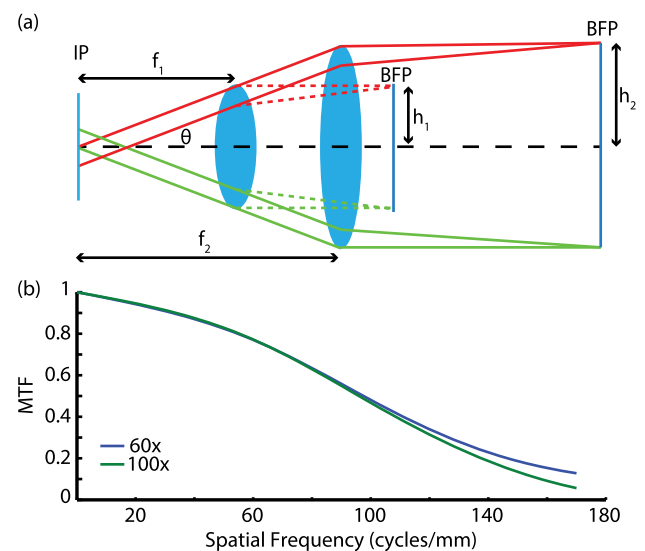
Fig. 4. Effect of magnification on Fourier image size and resolution. (a) Schematic demonstrating how, for a given NA, the objective's BFP is larger for smaller nominal magnifications, where f is the effective focal length, d is the semidiameter of the BFP image, and θ is the half angle determined by the NA of the objective. (b) Comparison of modulation transfer functions for the imaging configuration shown in Fig. 1(a) using 60× and 100× Nikon 1.4 NA Plan-Apo objectives.

the image plane for a sine wave object of a given spatial frequency.) Specifically, we plot the MTF for two Nikon objectives of the same NA but different magnifications (objectives 3 and 4 in Table 1). Note that not only do these two objectives have the same NA, but their specifications came from the same patent [50], making them the ideal comparison. As can be seen in Fig. 4(b), both objectives have a very similar MTF (and therefore comparable angular resolutions). Thus, the lower magnification objective maintains the BFP image quality while increasing its size. (However, it is important to note that the smaller BFP images from high-magnification objectives may still be desirable when working with low-light samples, e.g., weak single emitters).

C. Vignetting Reductions of Effective NA

Although these objectives were all designed for low-distortion wide-field imaging, they still suffer from reduced throughput at the edges of the field of view. For real-space imaging, this simply leads to a darker image at the edges than in the center. However, for Fourier imaging, vignetting decreases the observed intensity (collection efficiency) at large angles when imaging the full field of view. This, in turn, can lead to quantitatively different results when fitting the resulting radiation pattern. Thus, it is important to consider the effect of the collection area (which is often linked to the excitation spot size).

For collection from a 1-μm confocal region at the center of the field of view, vignetting is negligible, and all objectives transmit essentially 100% of the rays up to their full NA.
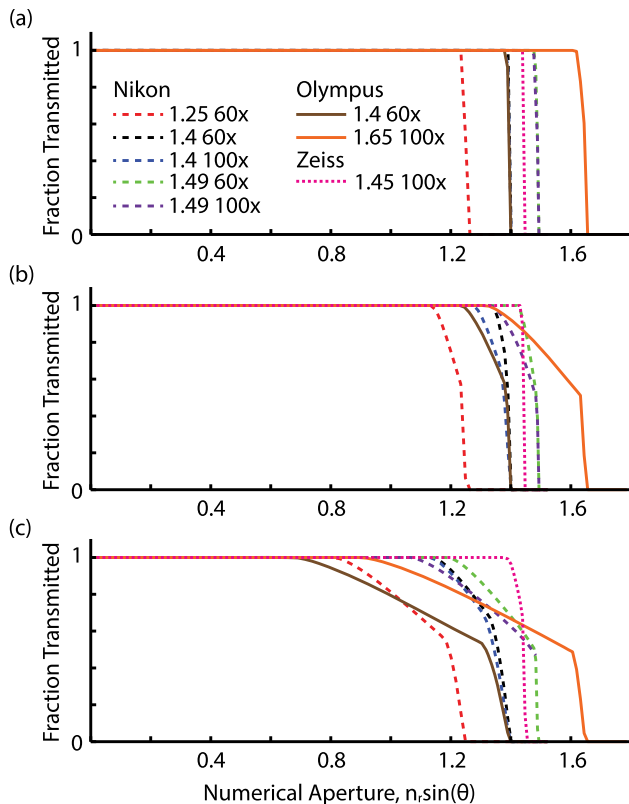
However, for wide-field collection, almost all objectives experience serious vignetting far short of their designed NA. To illustrate this, we plot the fraction of transmitted rays in Fig. 5 for three different collection areas ranging from a 10-μm diameter area in Fig. 5(a) to a 100-μm diameter area in Fig. 5(b) to the specified full field in Fig. 5(c). (Note that the full-field size depends on the manufacturer and magnification, because fields are generally specified by image rather than object size. Nikon and Olympus specify the full field to be a 22-mm image, whereas Zeiss specifies a 25-mm image.) While the vignetting effects within a 10-μm central area are minor, it is clear from Fig. 5 that increasing the field beyond 100 μm (or operating farther than 50 μm from the center of the field) will reduce the effective NA and can distort the Fourier image. Thus, although wide-field excitation of a fluorescent sample can greatly improve the signal-to-noise ratio, it will lead to an undesirable quantitative modification to the Fourier image in almost all microscope objectives and should therefore be avoided.

5. COMPARATIVE ANALYSIS OF IMAGING CONFIGURATIONS

From the analysis in Section 4, we have determined that the best choice for Fourier-space imaging is a plan-corrected apochromatic objective with a low magnification and a high NA. (Although all calculations were done at the d-line and therefore chromatic aberrations were not considered, the specific objectives that performed the best in our modeling were Plan-Apos. We would also recommend the use of apochromatic objectives in general, because the majority of fluorescence experiments involve broadband emitters.) With this in mind, we will now consider the relative performance of the four imaging configurations shown in Fig. 1. To compare these four configurations, we use the 60× 1.4 NA Nikon Plan-Apo objective and extract the field curvature and apodization factor at the detector plane. (As mentioned above, the apodization factor is often the only modification used to account for the optical setup in the literature.) As can be seen in Fig. 6(a), the apodization factors are nearly identical for all four configurations. However, Fig. 6(b) shows clear differences in the field curvatures. The

Fig. 5. Fraction of light transmitted for (a) 10-μm spot, (b) 100-μm spot, and (c) full field of view for the objectives listed in Table 1 using the imaging configuration shown in Fig. 1(a).
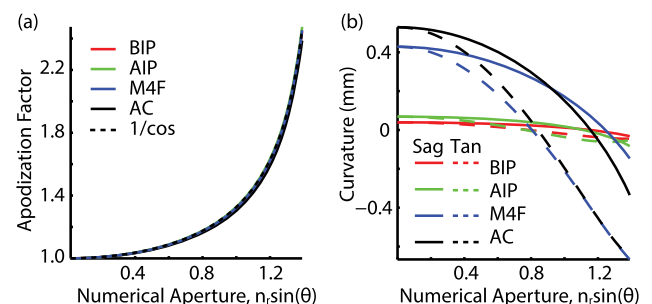
Fig. 6. Comparison of different Fourier imaging configurations with a Nikon 1.4 NA 60× objective. BIP, AIP, M4F, and AC correspond to the configurations shown in Figs. 1(a)–1(d), respectively. (a) Apodization factor for each configuration shown together with the ideal $1/\cos(\theta)$ apodization factor (dashed black line) for a system obeying the Abbe sine condition. (b) Sagittal and tangential field curvature as a function of field angle for the four configurations shown in Fig. 1.

field curvature is plotted in units of mm as the distance between the paraxial image plane and the real image plane as a function of $n_r \sin(\theta)$. While the AIP and BIP configurations have field curvatures on the order of 0.1 mm, the M4F and AC relay configurations exhibit curvature on the order of 1 mm. Therefore, it seems that the simpler AIP and BIP configurations may be slightly better, but given the small curvature (i.e., ≤1.3 mm) for all systems, it is not clear that this would lead to a significant imaging improvement.

The choice between the four Fourier imaging configurations in Fig. 1 is often limited by practical constraints. For example, it is often useful to place additional optics (e.g., polarizers, beamsplitters, filters) in the light path. Making the focal length of the Bertrand lens as long as possible can also be desirable, because it makes the BFP image on the detector larger and therefore reduces pixelation. Thus, despite being the simplest modification to a standard microscope, the BIP configuration in Fig. 1 is overly restrictive. Requiring the detector to be at the exit port image plane puts significant limits on the focal length of the Bertrand lens and leaves little room for other optical components. The AIP configuration alleviates both of these issues, but it cannot be used to obtain real-space images at the same detector plane. Finally, the M4F and AC relay configurations are the most flexible in magnification and allow for the removal or replacement of lenses to obtain real-space images. However, this increased flexibility comes at the cost of increased field curvature as well as increased complexity and associated tolerancing errors.

Interestingly, there is one other place where we have access to the beam path in a standard inverted microscope, namely, in the "infinity" space between the objective and tube lens. Although this space is typically occupied by excitation and emission filters, these are easily removed and Fourier imaging optics can be put in their place. The advantage of this setup is that the Bertrand lens, which now effectively acts as a tube lens, can be placed such that it directly focuses on the objective's

BFP, as shown in Fig. 7(a). This configuration combines the simplicity of the one-lens configurations in Figs. 1(a) and 1(b) and the BFP magnification flexibility of the relay configurations in Figs. 1(c) and 1(d) without curvature or tolerancing complications. As can be seen by a comparison of Figs. 7(b) and 7(c) to Figs. 3(c) and 3(f), tolerancing errors are greatly reduced when the Bertrand lens is placed before the tube lens. This is primarily due to the fact that the Bertrand lens is now directly imaging the back-focal-plane of the objective and therefore forms an infinite conjugate pair with the tube lens, whereas in all other configurations they form a finite conjugate pair.

Importantly, the configuration shown in Fig. 7(a) also provides a major advantage for system alignment, because deviations in the position of the Bertrand lens cause almost pure defocus. In the four common configurations shown in Fig. 1, movement of the Bertrand lens leads to both defocus and distortion, and it is distortion changes near the pupil edge that often produce the sharpest features during BFP alignment. However, when positioning the Bertrand lens in infinity space, the lack of distortion effects means that sharp features in the resulting Fourier image do correspond to good focus and thus proper alignment.

6. CONCLUSION

In conclusion, we have used patent information to model a range of microscope objectives in order to determine the ideal Fourier-space imaging setup. We have shown that, despite the significantly larger angles available to TIRF objectives, large deviations from ideal apodization can lead to severely aberrated Fourier images, especially for commonly used imaging configurations. It is therefore best to use a high-NA, Plan-Apo objective with a low magnification. Also, despite the gains in signal-to-noise when collecting from the full field of view, vignetting leads to an undesirable decrease in throughput at high angles and should therefore be avoided by using on-axis small-area collection. Finally, when using a standard commercially available microscope, the choice of imaging configuration outside the microscope is primarily a practical concern. However, with simple modifications, placing a lens between the objective and tube lens can significantly improve imaging performance and simplify the alignment process. We hope that these results, together with the tabulated surface data in Appendices A and B and the Zemax models in Ref. [41], will help advance the use of Fourier microscopy in nano-optics and nanophotonics. We also hope the methods and analysis presented here will be of interest to other fields, such as biological imaging, where complete models of microscope objectives and systems could help optimize high-resolution techniques.

Fig. 7. (a) Schematic of the Fourier microscopy configuration where a Bertrand lens is placed before the tube lens, along with apodization factor as a function of Bertrand lens position for (b) a Nikon 1.4 NA, 60× Plan-Apo objective and (c) a Nikon 1.49 NA, 60× TIRF objective. A significant improvement in tolerancing errors can be seen by a comparison to Figs. 3(c) and 3(f).

APPENDIX A: TUBE LENS SURFACE SPECIFICATIONS

Listed in Tables 2–4 are the specifications for the most likely implementations of Nikon, Olympus, and Zeiss tube lenses inferred from the patent literature, where r is the radius of curvature, d is the thickness, h is the semidiameter height, and Mfr is the glass manufacturer. (Semidiameters are set to the smallest clear aperture measured from actual tube lenses.)
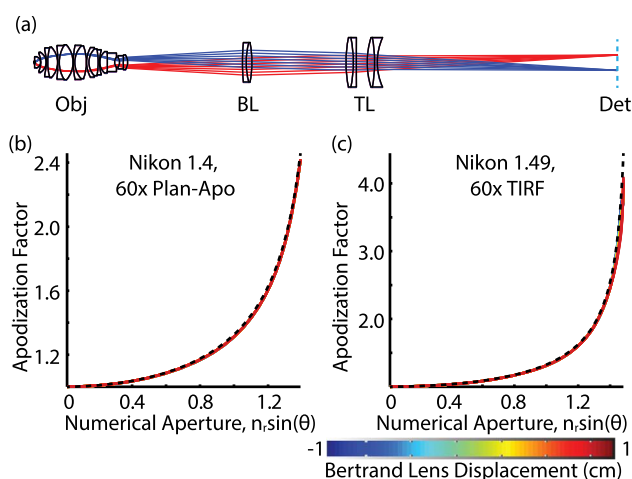
Table 2. Tube Lens from Nikon Patents [42,46–55]

Surf	r (mm)	d (mm)	h (mm)	Glass	Mfr
1	75.043	5.1	15.9385	E-SK10	Hikari
2	−75.043	2	15.9385	J-LAF7	Hikari
3	1600.58	7.5	15.9385		
4	50.256	5.1	15.9385	BASF6	Schott
5	−84.541	1.8	15.9385	KZFH1	Hikari
6	36.911	168.4117	15.9385		

Table 3. Tube Lens from Olympus Patents [56–62]

Surf	r (mm)	d (mm)	h (mm)	Glass	Mfr
1	68.7541	7.7321	13.97	S-FSL5	Ohara
2	−37.5679	3.4742	13.97	H-ZLAF52	CDGM
3	−102.8477	0.6973	13.97		
4	84.3099	6.0238	13.97	S-LAH60	Ohara
5	−50.71	3.0298	13.97	BPH35	Ohara
6	40.6619	156.9522	13.97		

Table 4. Tube Lens from Zeiss Patents [63–65]

Surf	r (mm)	d (mm)	h (mm)	Glass	Mfr
1	189.417	10.9	12.5	N-BALF4	Schott
2	−189.417	160.7711	12.5		

APPENDIX B: OBJECTIVE SURFACE SPECIFICATIONS

Listed in Tables 5–12 are the specifications for the microscope objectives listed in Table 1, where the notation is the same as described above in Appendix A. Note that for surfaces where an exact glass match could not be obtained (and for the immersion oil for every objective), the index and Abbe number are given at the d-line instead.

Table 5. 60×, 1.4 NA Objective from Nikon Patent [50]

Surf	r (mm)	d (mm)	h (mm)	Glass	Mfr
1	Infinity	0.17	0.183	1.52216, 58.80	
2	Infinity	0.15	0.39834	1.51536, 41.36	
3	Infinity	0.65	0.76209	S-NSL3	Ohara
4	−1.332	3.6	1.0598	LASF35	Schott
5	−3.716	0.1	3.6153		
6	−13.716	3.75	5.6585	GFK70	Sumita
7	−7.247	0.1	6.4791		
8	−27.891	1	7.8796	J-F5	Hikari
9	34.23	6.8	9.2544	GFK70	Sumita
10	−13.453	0.15	9.7985		
11	−84.754	1	10.2849	J-KZFH1	Hikari
12	20.048	9.4	10.8992	LITHO-CAF2	Schott
13	−16.266	0.15	11.288		
14	47.671	1.1	11.0093	J-KZFH1	Hikari
15	14.802	8	10.5143	LITHO-CAF2	Schott
16	−28.664	0.1	10.4895		
17	18.671	1.6	9.5306	J-KZFH1	Hikari
18	11.816	6.3	8.6046	LITHO-CAF2	Schott
19	−48.478	1	8.0904	1.526820, 51.35	
20	25.246	0.15	7.4167		
21	8.784	5.2	6.9181	GFK70	Sumita
22	−238.404	5	6.0015	S-LAH63	Ohara
23	4.823	3.4	3.2407		
24	−4.801	2.6	3.1155	S-LAH63	Ohara
25	204.674	3	4.2684	FD60-W	Hoya
26	−8.172	4.7147			

Table 6. 100×, 1.4 NA Objective from Nikon Patent [50]

Surf	r (mm)	d (mm)	h (mm)	Glass	Mfr
1	Infinity	0.17	0.11	1.52216, 58.80	
2	Infinity	0.15	0.39664	1.51536, 41.36	
3	Infinity	0.6	0.75712	S-NSL3	Ohara
4	−1.113	3.3	0.94294	LASF35	Schott
5	−3.32	0.1	3.2671		
6	−12.476	3.261	5.1827	J-PSK03	Hikari
7	−6.818	0.15	5.9356		
8	−28.872	1	7.1835	1.52682, 51.35	
9	20.752	7.77	8.6544	J-FKH1	Hikari
10	−12.157	0.2	9.2943		
11	−151.459	1	9.7384	F5	Schott
12	18.68	8.227	10.1252	LITHO-CAF2	Schott
13	−16.862	0.2	10.4318		
14	25.434	1	10.0854	J-KZFH1	Hikari
15	11.981	7.597	9.4033	LITHO-CAF2	Schott
16	−28.918	0.2	9.2799		
17	13.722	1.5	8.04	LAF7	Hoya
18	9.019	5.74	7.0106	LITHO-CAF2	Schott
19	−24.314	1.5	6.5153	KZFH2	Hikari
20	20.929	13.659	5.7806		
21	−115.034	1	3.3347	M-TAF1	Hoya
22	7.657	3	3.1723	H-ZF7L	NHG
23	−7.822	1	3.0012	M-TAF1	Hoya
24	11.351	2.7873			

Table 7. 60×, 1.25 NA Objective from Nikon Patent [54]

Surf	r (mm)	d (mm)	h (mm)	Glass	Mfr
1	Infinity	0.17	0.213	1.5244, 54.30	
2	Infinity	0.25	0.544	1.3326, 55.90	
3	−10	0.63	0.82735	LITHOSIL-Q	Schott
4	−1.051	2.82	0.94768	LAH55	Ohara
5	−2.921	0.1	2.8684		
6	−12.431	2.75	4.5036	GFK68	Sumita
7	−6.681	0.15	5.2569		
8	−63.897	1	6.4222	S-NSL36	Ohara
9	13.457	8.85	7.7123	E-FKH1	Hikari
10	−11.96	0.2	8.6884		
11	−636.078	1	8.9946	LAH59	Ohara
12	17.16	9.05	9.1801	LITHO-CAF2	Schott
13	−13.417	0.2	9.748		
14	17.111	1.2	9.3754	YGH51	Ohara
15	11.17	6.9	8.6363	LITHO-CAF2	Schott
16	−26.536	0.6	8.4528		
17	27.985	1.1	7.3624	LAH59	Ohara
18	20.792	4.5	6.939	LITHO-CAF2	Schott
19	−13.585	1	6.3993	LAH59	Ohara
20	46.225	0.2	6.0693		
21	7.409	5.9	5.828	E-FKH1	Hikari
22	−28.987	4.6	4.6985	BSM81	Ohara
23	3.708	2.9	2.545		
24	−4.496	4.4	2.4988	J-PSK03	Hikari
25	36.446	3.7	3.6535	FL7	Hoya
26	−7.761	4.1654			

Table 8.   60×, 1.49 NA Objective from Nikon Patent [42]

Surf	r (mm)	d (mm)	h (mm)	Glass	Mfr
1	Infinity	0.17	0.2085	1.52210, 58.8000	
2	Infinity	0.13	0.81893	1.51299, 40.6812	
3	Infinity	0.75	1.5517	S-NSL3	Ohara
4	−2.243	3.85	1.6556	S-LAH79	Ohara
5	−3.827	0.1	3.827		
6	−23.274	5	7.0632	GFK68	Sumita
7	−8.761	0.15	7.8999		
8	−38.045	1	9.0961	E-F2	Hikari
9	16.326	11	10.819	GFK70	Sumita
10	−15.9	0.15	11.4868		
11	331.735	1	11.4259	N-KZFS8	Schott
12	17	10.4	11.3175	LITHO-CAF2	Schott
13	−17.778	0.15	11.6131		
14	34.108	1	10.8098	N-KZFS5	Schott
15	16.2	5.6	10.2122	LITHO-CAF2	Schott
16	−103.612	1	10.0258		
17	17	4.1	9.0895	LITHO-CAF2	Schott
18	−129.879	1	8.6885	N-KZFS5	Schott
19	21.365	0.15	7.9004		
20	9.002	6.1	7.3838	J-PSK03	Hikari
21	−48.082	2.65	6.3398	J-LASF015	Hikari
22	5.9	4.45	4.1233		
23	−6.584	1	3.9245	S-LAH66	Ohara
24	20.8	3.4	4.5938	J-SF03	Hikari
25	−11.342	4.9719			

Table 9.   100×, 1.49 NA Objective from Nikon Patent [42]

Surf	r (mm)	d (mm)	h (mm)	Glass	Mfr
1	Infinity	0.17	0.125	1.52210, 58.8000	
2	Infinity	0.13	0.819	1.51299, 40.6812	
3	Infinity	0.93	1.5517	KF6	Schott
4	−2.322	3.95	1.8188	S-LAH79	Ohara
5	−3.939	0.15	3.9337		
6	−38.362	4.3	7.7336	GFK68	Sumita
7	−9.799	0.1	8.1798		
8	255.173	1	9.6314	N-KZFS5	Schott
9	16.559	7.5	10.3719	GFK70	Sumita
10	−20.805	0.15	10.5917		
11	232.841	2.7	10.7235	GFK70	Sumita
12	−123.237	1	10.7408	E-LAF11	Hikari
13	24.361	7.3	10.8094	LITHO-CAF2	Schott
14	−17.837	1	10.9498		
15	40.318	1	10.1101	N-KZFS8	Schott
16	11.663	8.3	9.2935	LITHO-CAF2	Schott
17	−18.121	0.2	9.3089		
18	12.026	1.2	7.7885	S-LAH63	Ohara
19	8.972	6	6.9603	LITHO-CAF2	Schott
20	−23.203	0.9	6.3056	N-SK14	Schott
21	19.497	0.2	5.5824		
22	6.568	5	5.0979	E-FKH1	Hikari
23	−33.082	2.5	3.8578	S-LAH66	Ohara
24	4.005	3	2.4296		
25	−4.235	2	2.1726	N-LAK33B	Schott
26	8.775	3.3	2.668	J-SF03	Hikari
27	−10.282	3.0054			

Table 10.   60×, 1.4 NA Objective from Olympus Patent [56]

Surf	r (mm)	d (mm)	h (mm)	Glass	Mfr
1	Infinity	0.17	0.221	1.521000, 56.020000	
2	Infinity	0.14	0.778	1.515480, 43.100000	
3	Infinity	0.6	0.73811	BSL7	Ohara
4	−1.8192	3.84	1.1653	LAH58	Ohara
5	−3.2177	0.15	3.2172		
6	−20.4857	2.1418	4.7439	N-PSK58	Schott
7	−8.7588	0.3	5.1808		
8	11.0685	5.3	6.3291	FPL51	Ohara
9	−10.4406	1	6.2509	BPM4	Ohara
10	18.9938	4.5	6.237	FPL53	Ohara
11	−17.4921	0.15	6.3246		
12	25.511	1	6.0815	BPH40	Ohara
13	6.4981	6.5	5.5195	FPL53	Ohara
14	−16.9602	1	5.638	BPH50	Ohara
15	−37.6734	0.3	5.7893		
16	8.7662	3.1	5.9715	FPL52	Ohara
17	145.8837	0.15	5.7691		
18	7.866	5.734	5.13	PHM52	Ohara
19	−8.8483	1	3.5547	BPH40	Ohara
20	3.0648	3.2	2.2843		
21	−3.4631	2.0409	2.1276	BPH50	Ohara
22	270.3729	6.7011	2.8398	TIH6	Ohara
23	−8.4836	4.2064			

Table 11.   100×, 1.65 NA Objective from Olympus Patent [58]

Surf	r (mm)	d (mm)	h (mm)	Glass	Mfr
1	Infinity	0.17	0.11	S-YGH52	
2	Infinity	0.1289	0.81	1.780350, 19.0701	
3	Infinity	0.51	0.7276	S-YGH52	Ohara
4	−3.437	2.17	1.3207	LAH58	Ohara
5	−2.2093	0.1325	2.2008		
6	−10.9949	2.45	3.668	LAH58	Ohara
7	−5.8271	0.1997	4.3677		
8	12.675	5.32	5.3696	FPL53	Ohara
9	−22.9089	1.2	5.5172	LAL8	Ohara
10	10.1935	7.3	5.7944	FPL53	Ohara
11	−9.0192	0.2	6.4719		
12	8.0162	4.8	6.0812	PHM52	Ohara
13	−20.6259	1.25	5.5464	BPH50	Ohara
14	5.2036	1	4.0885		
15	5.6171	5.4	4.3743	FPL53	Ohara
16	−6.1286	1.2	3.9893	BPH35	Ohara
17	−28.4328	0.2334	3.8486		
18	8.1214	4.9	3.5963	FPL53	Ohara
19	−13.9811	2.6848	2.5328	BPM4	Ohara
20	6.8433	1.3	1.8288		
21	−2.6403	3.0112	1.7564	BPH35	Ohara
22	14.3617	2.54	2.6551	S-TIH6	Ohara
23	−7.4872	2.9716			

Table 12.   100×, 1.45 NA Objective from Zeiss Patent [66]

Surf	r (mm)	d (mm)	h (mm)	Glass	Mfr
1	Infinity	0.17	0.125	1.52216, 58.50	
2	Infinity	0.12	0.675	1.51536, 41.36	
3	Infinity	0.6	1	N-BK7	Schott
4	−1.2579	2.5	1.08	N-LASF31	Schott
5	−2.778	0.1	2.77		
6	−6.5423	3.64	4.345	N-FK51	Schott
7	−4.9407	0.1	4.94		
8	−44.666	3.09	7.15	N-PK51	Schott
9	−11.14	0.103	7.45		
10	−139.25	1.11	7.92	N-KZFS4	Schott
11	12.23	7.76	8.53	N-PK51	Schott
12	−13.925	0.1	8.77		
13	21.754	4.87	8.25	CAF2	Infrared
14	−15.961	1.16	8.035	N-KZFS4	Schott
15	9.8584	4.87	7.365	N-PK51	Schott
16	−51.958	0.205	7.315		
17	6.7777	5.83	6.5	N-PK51	Schott
18	−93.056	1.1	5.915	N-KZFS4	Schott
19	3.5485	1.306	3.37		
20	4.5281	4.85	3.425	N-PK51	Schott
21	3.759	1.907	2.255		
22	−3.1612	1.92	2.235	SF2	Schott
23	−2.8175	0.73	2.6	N-FK51	Schott
24	−8.1748	2.915			

REFERENCES

1. M. A. Lieb, J. M. Zavislan, and L. Novotny, "Single-molecule orientations determined by direct emission pattern imaging," J. Opt. Soc. Am. B **21**, 1210–1215 (2004).
2. S. Castelletto, I. Aharonovich, B. Gibson, B. Johnson, and S. Prawer, "Imaging and quantum-efficiency measurement of chromium emitters in diamond," Phys. Rev. Lett. **105**, 217403 (2010).
3. T. H. Taminiau, S. Karaveli, N. F. van Hulst, and R. Zia, "Quantifying the magnetic nature of light emission," Nat. Commun. **3**, 979 (2012).
4. S. Karaveli, S. Wang, G. Xiao, and R. Zia, "Time-resolved energy-momentum spectroscopy of electric and magnetic dipole transitions in Cr³⁺:MgO," ACS Nano **7**, 7165–7172 (2013).
5. J. A. Schuller, S. Karaveli, T. Schiros, K. He, S. Yang, I. Kymissis, J. Shan, and R. Zia, "Orientation of luminescent excitons in layered nanomaterials," Nat. Nanotechnol. **8**, 271–276 (2013).
6. A. S. Backer, M. P. Backlund, M. D. Lew, and W. E. Moerner, "Single-molecule orientation measurements with a quadrated pupil," Opt. Lett. **38**, 1521–1523 (2013).
7. C. M. Dodson, J. A. Kurvits, D. Li, and R. Zia, "Wide-angle energy-momentum spectroscopy," Opt. Lett. **39**, 3927–3930 (2014).
8. A. Drezet, A. Hohenau, D. Koller, A. Stepanov, H. Ditlbacher, B. Steinberger, F. Aussenegg, A. Leitner, and J. Krenn, "Leakage radiation microscopy of surface plasmon polaritons," Mater. Sci. Eng. B **149**, 220–229 (2008).
9. C. Huang, A. Bouhelier, G. C. D. Francs, A. Bruyant, A. Guenot, E. Finot, J.-C. Weeber, and A. Dereux, "Gain, detuning, and radiation patterns of nanoparticle optical antennas," Phys. Rev. B **78**, 155407 (2008).
10. P. Bharadwaj, A. Bouhelier, and L. Novotny, "Electrical excitation of surface plasmons," Phys. Rev. Lett. **106**, 226802 (2011).
11. I. Sersic, C. Tuambilangana, and A. F. Koenderink, "Fourier microscopy of single plasmonic scatterers," New J. Phys. **13**, 083019 (2011).
12. T. Shegai, S. Chen, V. D. Miljković, G. Zengin, P. Johansson, and M. Käll, "A bimetallic nanoantenna for directional colour routing," Nat. Commun. **2**, 481 (2011).
13. T. Shegai, V. D. Miljkovic, K. Bao, H. Xu, P. Nordlander, P. Johansson, and M. Käll, "Unidirectional broadband light emission from supported plasmonic nanowires," Nano Lett. **11**, 706–711 (2011).
14. F. B. Arango, A. Kwadrin, and A. F. Koenderink, "Plasmonic antennas hybridized with dielectric waveguides," ACS Nano **6**, 10156–10167 (2012).
15. B. Buchler, T. K. C. Hettich, and V. Sandoghdar, "Measuring the quantum efficiency of the optical emission of single radiating dipoles using a scanning mirror," Phys. Rev. Lett. **95**, 063003 (2005).
16. A. L. Mattheyses and D. Axelrod, "Fluorescence emission patterns near glass and metal-coated surfaces investigated with back focal plane imaging," J. Biomed. Opt. **10**, 054007 (2005).
17. W. Tang, E. Chung, Y. Kim, P. So, and C. Sheppard, "Effects of using a metal layer in total internal reflection fluorescence microscopy," Appl. Phys. A **89**, 333–335 (2007).
18. A. G. Curto, G. Volpe, T. H. Taminiau, M. P. Kreuzer, R. Quidant, and N. F. van Hulst, "Unidirectional emission of a quantum dot coupled to a nanoantenna," Science **329**, 930–933 (2010).
19. H. Aouani, O. Mahboub, N. Bonod, E. Devaux, E. Popov, H. Rigneault, T. W. Ebbesen, and J. Wenger, "Bright unidirectional fluorescence emission of molecules in a nanoaperture with plasmonic corrugations," Nano Lett. **11**, 637–644 (2011).
20. K. Lee, X. Chen, H. Eghlidi, P. Kukura, R. Lettow, A. Renn, V. Sandoghdar, and S. Götzinger, "A planar dielectric antenna for directional single-photon emission and near-unity collection efficiency," Nat. Photonics **5**, 166–169 (2011).
21. T. Shegai, B. Brian, V. D. Miljkovic, and M. Käll, "Angular distribution of surface-enhanced raman scattering from individual au nanoparticle aggregates," ACS Nano **5**, 2036–2041 (2011).
22. T. Shegai, P. Johansson, C. Langhammer, and M. Käll, "Directional scattering and hydrogen sensing by bimetallic Pd-Au nanoantennas," Nano Lett. **12**, 2464–2469 (2012).
23. R. Wagner, L. Heerklotz, N. Kortenbruck, and F. Cichos, "Back focal plane imaging spectroscopy of photonic crystals," Appl. Phys. Lett. **101**, 081904 (2012).
24. W. Zhu, D. Wang, and K. B. Crozier, "Direct observation of beamed Raman scattering," Nano Lett. **12**, 6235–6243 (2012).
25. S. A. Guebrou, C. Symonds, E. Homeyer, J. Plenet, Y. N. Gartstein, V. M. Agranovich, and J. Bellessa, "Coherent emission from a disordered organic semiconductor induced by strong coupling with surface plasmons," Phys. Rev. Lett. **108**, 066401 (2012).
26. N. Hartmann, G. Piredda, J. Bertelot, G. C. des Francs, A. Bouhelier, and A. Hartschuh, "Launching propagating surface plasmon polaritons by a single carbon nanotube," Nano Lett. **12**, 177–181 (2012).
27. N. Hartmann, D. Piatkowski, R. Ciesielski, S. Mackowski, and A. Hartschuh, "Radiation channels close to a plasmonic nanowire visualized by back focal plane imaging," ACS Nano **7**, 10257–10262 (2013).
28. D. Wang, W. Zhu, M. D. Best, J. P. Camden, and K. B. Crozier, "Directional raman scattering from single molecules in the feed gaps of optical antennas," Nano Lett. **13**, 2194–2198 (2013).
29. A. G. Curto, T. H. Taminiau, G. Volpe, M. P. Kreuzer, R. Quidant, and N. F. van Hulst, "Multipolar radiation of quantum emitters with nanowire optical antennas," Nat. Commun. **4**, 1750 (2013).
30. I. M. Hancu, A. G. Curto, M. Castro-López, M. Kuttge, and N. F. van Hulst, "Multipolar interference for directed light emission," Nano Lett. **14**, 166–171 (2014).
31. Y. Chen, D. Zhang, L. Zhu, R. Wang, P. Wang, H. Ming, R. Badugu, and J. R. Lakowicz, "Tamm plasmon- and surface plasmon-coupled emission from hybrid plasmonic-photonic structures," Optica **1**, 407–413 (2014).

32. A. H. Schokker and A. F. Koenderink, "Lasing at the band edges of plasmonic lattices," Phys. Rev. B **90**, 155452 (2014).

33. L. Shi, T. Hakala, H. Rekola, J.-P. Martikainen, R. Moerland, and P. Törmä, "Spatial coherence properties of organic molecules coupled to plasmonic surface lattice resonances in the weak and strong coupling regimes," Phys. Rev. Lett. **112**, 153002 (2014).

34. G. Bulgarini, M. E. Reimer, M. B. Bavinck, K. D. Jöns, D. Dalacu, P. J. Poole, E. P. Bakkers, and V. Zwiller, "Nanowire waveguides launching single photons in a Gaussian mode for ideal fiber coupling," Nano Lett. **14**, 4102–4106 (2014).

35. C. I. Osorio, A. Mohtashami, and A. F. Koenderink, "K-space polarimetry of bullseye plasmon antennas," Sci. Rep. **5**, 9966 (2015).

36. A. Mohtashami, C. I. Osorio, and A. F. Koenderink, "Angle-resolved polarimetry measurements of antenna-mediated fluorescence," arXiv:1506.00140v1 (2015).

37. A. G. Curto, Stanford University, 450 Serra Mall, Stanford, CA 94305 (personal communication, 2015).

38. G. Zheng, R. Horstmeyer, and C. Yang, "Wide-field, high-resolution Fourier ptychographic microscopy," Nat. Photonics **7**, 739–745 (2013).

39. J. E. Curtis, B. A. Koss, and D. G. Grier, "Dynamic holographic optical tweezers," Opt. Commun. **207**, 169–175 (2002.)

40. J. Liang and M. F. Becker, "Spatial bandwidth analysis of fast backward Fresnel diffraction for precise computer-generated hologram design," Appl. Opt. **53**, G84–G94 (2014).

41. J. A. Kurvits, M. Jiang, and R. Zia, "Zemax (optical design) files of microscope objective, tube lens, and Fourier imaging setups," (figshare, 2015), http://dx.doi.org/10.6084/m9.figshare.1481270.

42. M. Mandai, "Immersion microscope objective lens," U.S. patent 7,046,451 B2 (May 6, 2006).

43. "Nikon Instruments wins R&D Magazine's top 100 new products of the year," http://www.nikoninstruments.com/About-Nikon/News-Room/US-News/Nikon-Instruments-Wins-R-D-Magazine-s-Top-100-New-Products-of-The-Year [Accessed July 9, 2015].

44. "Reducing hazardous substances in products," http://nikon.com/about/csr/environment/products/products_02/index.htm [Accessed June 30, 2015].

45. "Ohara corporate data," http://www.ohara-inc.co.jp/en/company/overview.html [Accessed June 30, 2015].

46. K. Watanabe, "Immersion-type microscope objectve lens," U.S. patent 5,798,869 A (August 25, 1998).

47. N. Furutake, "Immersion microscope objective lens system," U.S. patent 5,982,559 A (November 9, 1999).

48. S. Kudo, "Immersion microscope objective," U.S. patent 5,978,147 A (November 2, 1999).

49. N. Furutake, "Microscope objective lens," U.S. patent 6,128,139 (October 3, 2000).

50. K. Yamaguchi, "Immersion microscope objective lens," U.S. patent 6,519,092 B2 (February 11, 2003).

51. Y. Okuyama, "Liquid immersion type microscope objective lens," U.S. patent application 2003/0043473 A1 (March 6, 2003).

52. K. Watanabe, "Liquid immersion type microscope objective lens," U.S. patent 6,700,710 B2 (March 2, 2004).

53. K. Yamaguchi, "Immersion microscope objective lens," U.S. patent 7,262,922 B2 (August 28, 2007).

54. M. Yoshida, "Immersion type microscope objective lens," U.S. patent 7,889,433 B2 (February 15, 2011).

55. K. Yamaguchi, "Immersion microscope objective lens," U.S. patent 8,199,408 B2 (June 12, 2012).

56. T. Suzuki, "Immersion microscope objective," U.S. patent 5,517,360 A (May 14, 1996).

57. T. Suzuki, "Immersion microscope objective," U.S. patent 5,502,596 A (March 26, 1996).

58. T. Suzuki, "Immersion microscope objective," U.S. patent 5,659,425 A (August 19, 1997).

59. Y. Fujimoto and T. Kasahara, "Immersion objective lens system for microscope," U.S. patent 7,199,938 B2 (April 3, 2007).

60. H. Konishi, Y. Fujimoto, K. Kusaka, and T. Kasahara, "Immersion type microscope objective," U.S. patent 7,486,445 B2 (February 3, 2009).

61. T. Kasahara, "Immersion microscope objective and microscope using the same," U.S. patent application 2013/0271829 A1 (October 17, 2013).

62. T. Kasahara, "Immersion microscope objective and microscope with it," U.S. patent 8,358,469 B2 (January 22, 2013).

63. R. Wartmann and J. Sprenger, "Liquid immersion microscope objective," U.S. patent 7,133,212 B2 (November 7, 2006).

64. F. Muchel, "Tube lens unit with chromatically compensating effect," U.S. patent 7,289,271 B2 (October 30, 2007).

65. R. Shi, I. Fahlbusch, and W. Kleinschmidt, "Immersion microscope objective," U.S. patent 7,782,539 B2 (August 24, 2010).

66. M. Matthae, L. Schreiber, A. Faulstich, and W. Kleinscgmidt, "High aperture objective lens," U.S. patent 6,504,653 B2 (January 7, 2003).

67. C. Sheppard and M. Gu, "Imaging by a high aperture optical system," J. Mod. Opt. **40**, 1631–1651 (1993).